Improving GNSS-R Ocean Wind Speed Retrieval for the BF-1 Mission Using Satellite Platform Attitude Measurements

Chenxin Chen [ID], Xiaoyu Wang [ID], Zhao Bian, Haoyun Wei, Dongdong Fan, and Zhaoguang Bai

Abstract—The receive antenna gain is needed to accurately calibrate the normalized bistatistic radar cross section measured by the BF-1 mission, which is a global navigation satellite system reflectometry (GNSS-R) constellation of two microsatellites and the first Chinese GNSS-R satellite mission. The instability of the satellite platform is the main cause of receive antenna gain errors. To obtain a high precision gain value, a calibration method that remaps the ocean surface detection location to the receive antenna pattern using satellite platform attitude measurements is proposed in this article. Thirty-two orbits of delay Doppler maps data, which were greatly disturbed by the attitude, are selected to test the effectiveness of the proposed algorithm. The accuracy of wind speed retrieval is analyzed, and results show that the data calibration algorithm is effective in reducing the wind speed retrieval error. Compared with the un-calibrated data, the data subjected to the calibration algorithm show a significant improvement of 19.33% in correlation coefficient and average decreases of 30.91% and 42.57% in root-mean-square error and mean bias error, respectively. Moreover, the comparison highlights that the influence of the satellite platform attitude disturbance on wind speed retrieval is abated significantly. The proposed approach can effectively improve the quality of GNSS-R measurements, allowing for a better understanding of global weather abnormalities and generally improving weather forecasting.

Index Terms—BF-1 mission, Bistatic radar, delay Doppler map (DDM), geometric calibration, global navigation satellite system reflectometry (GNSS-R), ocean remote sensing, satellite attitude, wind speed retrieval.

I. INTRODUCTION

WINDS play a major role in every aspect of weather on earth. Ocean surface wind is an essential variable in marine environment monitoring and climate change study [1], the direct power of ocean wave formation, and the key power of regional and global ocean circulation [2]. Moreover, they

directly affect the turbulent exchanges of heat, moisture, gases, and other physical parameters between the atmosphere and the ocean [3]. In addition, using accurate inputs of ocean surface wind is crucial in wind resource assessment [4], hurricane center determination [5], and ocean surface heat flux product development [6]. To better understand the impact of winds on oceans and improve weather forecasting, satellite remote sensing, both active (such as scatterometer) and passive (such as radiometer), has been providing a significant understanding of the ocean by providing global observations [7], [8].

As a new type of ocean remote sensing method, GNSS-R, which combines active and passive remote sensing, has become a valid option, by measuring reflections off the ocean's surface through the signals transmitted from various GNSS constellations. This type of microwave reflectometers relies on the forward scattering measurements of opportunity signals in a bistatic configuration [9] and the signals contain wind speed information about the ocean surface [10]. The GNSS-R receiver measures the strength of the signal scattered by the earth's surface after the signal is selectively filtered by time delay and Doppler shift to create DDMs in the vicinity of the specular point. The measurement location is referred to as specular point, which is defined as the location where a signal sent by a GNSS reflects with equal angle of incidence and reflection on the surface of the earth back to the target satellite [11]. The *L*-band signals used by the GNSS-R satellite can effectively penetrate the atmosphere and are immune to weather conditions, thereby guaranteeing all-day and all-weather surveillance over the regions of interest [12]. Therefore, relative to other space-borne ocean wind sensors, the GNSS-R-based satellite can measure the ocean surface wind speed under heavy precipitation because of its low operating frequency and capture short-lived weather events due to the rapid sampling from using a constellation [13].

Using GNSS signals in a bistatic scatterometer configuration was first proposed in 1988 [14]. Subsequently, the reflected GPS signal was successfully received from space by the GPS receiver onboard U.K.'s disaster monitoring constellation satellite in 2003 [15], [16], which was used to demonstrate sensitivity to wind speed. This was followed by the U.K. TechDemoSat-1 (TDS-1) on-orbit demonstration mission in 2014 [17], and subsequently the NASA Cyclone Global Navigation Satellite System (CYGNSS) constellation was launched with the specific aim of observing the inner core of cyclones with high temporal

resolution in precipitating conditions in 2016 [18], which was used to further validate and develop GNSS-R ocean wind speed applications [19]. Additionally, China has also launched the BF-1 A/B satellites in 2019, which is part of the first Chinese GNSS-R satellite constellation for measuring global sea surface wind field and typhoon monitoring [20]. Providing high quality GNSS-R measurements that can reliably be used for ocean wind speed retrieval, and assimilation into numerical weather prediction models is primary aim of these GNSS-R missions. However, data quality is still the main obstacle affecting the accuracy of GNSS-R ocean wind retrieval. Various methods for improving data reliability have been developed and can be generally categorized into two groups: geometric calibration and quality control. For the former category, several improvements based on the observed on-orbit performance are applied to each GNSS-R raw science data for improving data quality. In general, accurate and robust geometric calibration of GNSS-R observations is a necessary first step to enable subsequent geophysical parameter retrievals [21]. The latter method uses quality control filters to detect and remove outlier measurements [22], and attitude errors, the signal-to-noise ratio (SNR), and the range corrected gain are often used as data quality control and filtering conditions [23], [24].

BF-1 mission geometric calibration converts the received power to bistatic radar cross section values by unwrapping the forward scattering model and using the external metadata, which are then normalized by the surface scattering area to arrive at an observation of the normalized bistatic radar cross section values [25]. The key part of the external metadata is the receive antenna pattern, which is a function of gain with respect to the off-nadir and azimuth angle, and determines the signal receive gain of earth's surface detection location. Therefore, the accuracy and precision of the receive antenna gain are significant to the geometric calibration and to the accuracy of the ocean surface wind determination. In general, the receiver antenna patterns on orbit calibration includes two aspects: the precision correction of the antenna patterns itself, and the position correction of the receiver point in the antenna patterns. The improved antenna patterns correction method used by CYGNSS was implemented by [25]. However, the latter is rarely mentioned in the literature. The receive antenna gain position correction mainly refers to the mapping position correction of the ocean detection location in the antenna pattern, and the mapping error of the receiver point in the receive antenna patterns is mainly caused by the attitude change of the satellite platform. The instability of the satellite platform has received extensive attention due to its great interference to data processing. Hammond et al. evaluated the wind speeds data during the three years of the TDS-1 mission. Their analyses revealed a significant temporal variability in monthly wind speed retrieval performance that is driven partly by the TDS-1 platform attitude uncertainty [26]. To derive a high-precision empirical geophysical model function (GMF) for ocean wind speed retrieval, Ruf and Balasubramaniam [24] discarded the training sample data with inaccuracies in the CYGNSS spacecraft attitude. Reynolds et al. [27] and Li et al. [28]. discarded cases in which the spacecraft has large attitude errors or attitude anomalies because these data may introduce uncertainties in the artificial neural network model training. However, these studies only showed that satellite platform attitude will affect the accuracy of wind speed retrieval, or to remove attitude anomalies measurements using quality control filters, but the use of platform attitude measurements for receive antenna gain calibration was not analyzed.

In this article, we develop a satellite platform attitude information based receive antenna gain calibration method for the ocean wind retrieval. Following this introduction, Section II presents brief overviews of the BF-1 mission, the materials used, and then describes the proposed calibration method. Section III presents the analysis of the effectiveness of the presented method, and Sections IV and V concludes this article with a summary and possible future work.

II. MATERIALS AND METHODS

A. BF-1 Mission

Two BF-1 satellites were launched into low earth orbit (with an altitude of approximately 579 km and at an orbit inclination of 45°) on June 5, 2019 [20]. The orbit can cover most areas of the typhoon tracks and ocean near China. Each satellite is equipped with a low-mass and -power GNSS-R receiver, which consists of a signal processing unit, two nadir-pointing (i.e., downward-pointing) antennas for collecting the GNSS signals scattered off of the ocean surface, and a single zenith-pointing (i.e., upward-pointing) antenna for collecting direct GNSS signals. The receiver collects reflected signals using a highly directional nadir antenna, with a peak gain of 14.6 dBi and a half beam width of 22° by 44° (3 dB).

Each BF-1 satellite carries a four-channel receiver that tracks and measures the GNSS signals reflected by the earth's surface from at most four different GNSS satellite transmitters, and the instrument outputs at most four raw DDM measurements every second. Thus, the constellation of two satellites can make up to at most eight simultaneous raw measurements per second. The raw DDMs are first processed into a geometric calibration product, and then the retrieval model is used to convert these observables into a wind speed product. The geometric product includes the calibrated NBRCS (stored in a signal box with five Doppler $\times$ seven delay bins) and other ancillary information and metadata, and the data are stored according to the orbit. The sizes of the delay and Doppler bin are 0.25 chip and 500 Hz, respectively, and the size of the signal box is -0.5–1 chip in the delay dimension and -1000–1000 Hz in the Doppler dimension of a compressed DDM. The satellite platform's attitude angle accuracy has been used to estimate the error of geometric calibration [29], but the attitude information has not been considered in the geometric data calibration of the BF-1 mission.

B. Materials

1) Platform Attitude Data: Since BF-1 satellites were launched into orbit, their platform attitude has changed to varying degrees. The standard deviations of the reported platform orientation (pitch, roll, and yaw) of BF-1 A and BF-1 B over one year are plotted in Fig. 1. These results show clear changes
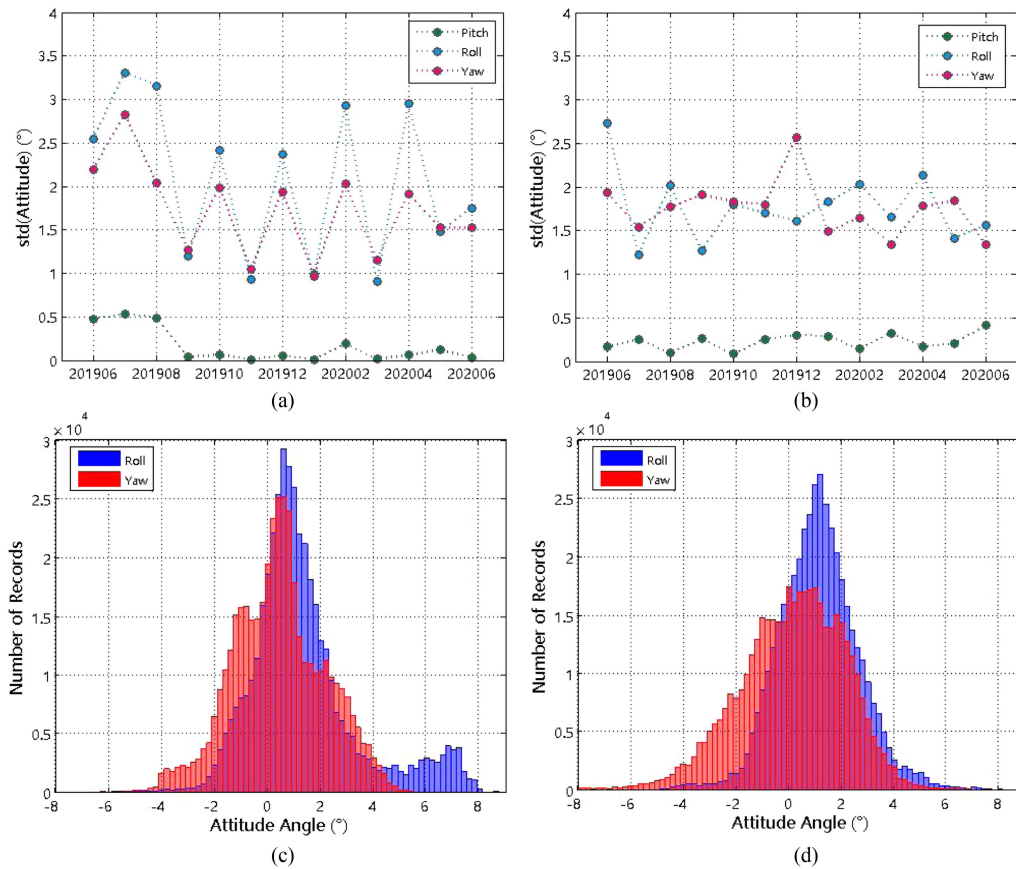
Fig. 1. Temporal evolution of BF-1 satellites attitude fluctuations within approximately one year after launch shown as the standard deviation and their histogram distribution (given that the pitch attitude fluctuation is not obvious, only roll and yaw are counted here). (a) and (c) For the BF-1 A satellite, (b) and (d) For the BF-1 B satellite.

in the stability of the platform attitude over time and periodic or irregular changes.

Three attitude data of the satellite platform, namely, pitch, roll, and yaw, were recorded in XLSX format after being received by the ground receiving station. However, these attitude data were recorded in the form of reduced sampling frequency, and two sampling frequencies were adopted, that is, samples were taken every 2 s and every 6 min. Fig. 2(a) shows the discrete attitude data distribution of the BF-1A satellite in one day, and the large discrete data points adopted the 6 min sampling strategy, while the smaller one adopted the 2 s sampling. To analyze the attitude of the satellite platform at the time of DDM data acquisition, these discrete attitude data were then interpolated using cubic splines interpolation to a resolution of 1 s. Fig. 2(b)–(d) shows the interpolation results of pitch, roll, and yaw, respectively, and the attitude corresponding to orbit 04708 (selected as one of the DDM data in this article) is displayed in bold red font.

Taking the attitude of the BF-1A satellite on April 14, 2020 as an example (see Fig. 2), the absolute attitude deviation value greater than 5° accounts for 21.34% of the roll and 16.4% of the yaw.

The integrated attitude error, which is calculated based on the three attitude components of the satellite platform, is used to characterize the disturbance attitude. This variable is given by the following equation:

$$E_{\text{atti}} = \sqrt{(\text{pitch})^2 + (\text{roll})^2 + (\text{yaw})^2}. \tag{1}$$

where E_{atti} is the integrated attitude error, and the pitch, roll, and yaw are the attitude components of the satellite platform.

2) DDM Data: To test the effectiveness of the proposed algorithm, the data greatly disturbed by the attitude of the satellite platform were selected as the test datasets. A total of 32 orbits of the BF-1A and BF-1B satellites in March and April 2020 were used, and only the ocean observable 50 km away from the coastline was selected. The measurements of full orbit and open ocean filtering were taken. In addition, to ensure high data quality, low gain data, which are mostly outside the 30° off-nadir of the antenna beam center, were excluded from the analysis. Therefore, the sample population for this analysis contains approximately 4.0×10^5 measurements.

A global map that overlaps with the 32 orbits' specular points is presented in Fig. 3, and Table I gives the basic information of the data used.

Given the large disturbance of satellite attitude to the Thirty-two orbits experimental data selected, the dynamic range of Integrated Attitude Error (E_{atti}) is large (see Fig. 4). The minimum
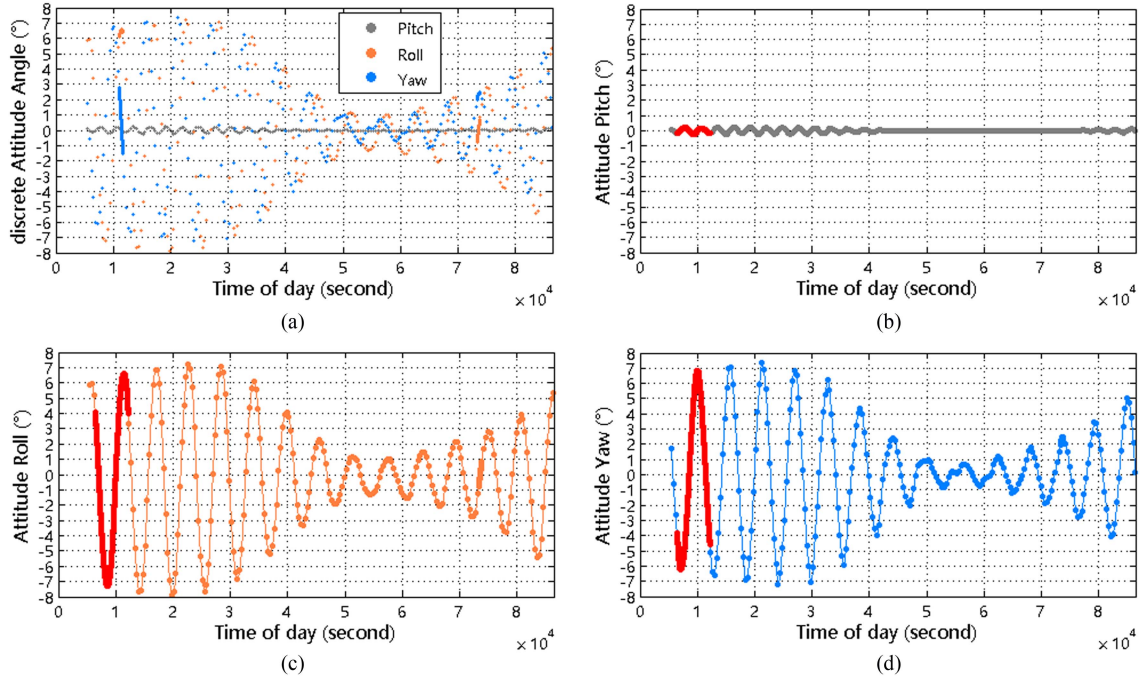
Fig. 2.   Temporal evolution of BF-1A satellite attitude fluctuations shown as the angle of (a) three discrete attitude and the interpolation results of (b) pitch, (c) roll, and (d) yaw within one day (April 14, 2020). Note that all parameters, except for pitch, show significant changes over time.

TABLE I
SELECTED DATA

| Products	Orbit	Date	Second of Day (s)	Pitch (°)	Roll (°)	Yaw (°)	$E_{atti}*100$ (rad)	Full orbit/ Ocean	Measure ments
1-BF-1A	04427	March 26	30014-35772	-0.05-0.04	-3.42-2.48	-2.93-3.55	4.11-6.475	21828/16165	11510
2-BF-1B	04429		30907-36665	-0.83-0.43	-3.58-4.87	-6.59-4.98	1.14-14.25	21840/16319	12370
3-BF-1A	04456	March 28	24197-29955	-0.08-0.07	-4.35-3.02	-3.58-4.64	5.23-8.24	21832/17854	13112
4-BF-1B	04457		19333-25091	-0.21-2.01	-3.68-5.41	-5.46-4.26	4.34-11.89	21832/15495	11736
5-BF-1A	04486	March 30	24139-29897	-0.12-0.10	-4.82-3.43	-3.92-5.16	5.84-9.34	21808/15877	11540
6-BF-1B	04495		65340-71098	-0.27-0.29	-1.63-3.01	-3.67-1.43	0.03-6.99	21844/16714	12583
7-BF-1A	04515	April 1	18325-24083	-0.16-0.13	-6.26-4.57	-5.25-6.49	7.63-11.50	21820/17992	13286
8-BF-1B	04516		13464-19222	-0.15-0.28	-3.81-4.32	-5.15-3.84	3.48-10.45	21808/16243	12021
9-BF-1A	04530	April 2	18296-24054	-0.19-0.13	-6.40-4.81	-5.40-6.72	7.90-11.73	21804/16875	12912
10-BF-1B	04533		24951-30709	-0.21-1.11	-6.12-4.09	-7.30-6.31	6.06-12.81	21828/15761	11910
11-BF-1A	04560	April 4	18240-23995	-0.22-0.18	-6.95-5.71	-5.97-7.16	9.32-12.60	21824/15610	11519
12-BF-1B	04561		13378-19133	-0.15-0.14	-4.59-3.88	-7.09-5.44	5.15-12.91	21844/17680	13785
13-BF-1A	04591	April 6	23940-29695	-0.25-0.25	-8.17-6.86	-7.34-8.08	11.49-14.32	21812/15920	12533
14-BF-1B	04591		13320-19078	-0.12-0.21	-4.04-3.26	-7.40-5.98	4.28-13.92	21816/16214	12688
15-BF-1A	04607	April 7	29665-35423	-0.23-0.21	-7.53-6.53	-7.17-7.12	11.09-13.16	21828/16380	13079
16-BF-1B	04607		19049-24807	-0.68-0.15	-3.90-2.15	-5.04-5.95	2.74-11.47	21832/15958	13328
17-BF-1A	04634	April 9	12332-18090	-0.31-0.28	-8.33-7.42	-7.13-7.82	10.97-14.76	21836/15780	12533
18-BF-1B	04647		76572-81681	-0.15-0.08	-2.11-1.88	-1.67-6.55	1.07-11.43	19380/12204	10218
19-BF-1A	04651	April 10	23819-29577	-0.30-0.29	-8.65-7.80	-7.80-8.36	12.51-15.10	21804/16681	14285
20-BF-1B	04650		7446-13204	-0.24-0.12	-4.84-5.60	-4.94-6.08	4.44-13.04	21820/16801	13266
21-BF-1A	04666	April 11	23789-29547	-0.25-0.25	-8.02-7.30	-7.25-7.55	12.07-14.01	21364/16440	12724
22-BF-1B	04677		76513-81729	-0.07-0.12	-2.51-1.80	-1.95-6.21	0.07-10.94	19753/12631	10358
23-BF-1A	04694	April 13	12213-17971	-0.23-0.22	-7.38-6.61	-6.24-7.02	10.51-12.93	21840/16028	12990
24-BF-1B	04696		13116-18874	-0.19-0.08	-5.67-3.68	-4.01-7.16	1.37-12.97	19072/13930	10647
25-BF-1A	04708	April 14	6426-12184	-0.21-0.20	-7.30-6.63	-6.21-6.87	9.74-12.75	21808/15986	12946
26-BF-1B	04709		1571-7329	-0.43-0.04	-4.76-3.79	-3.95-7.06	2.40-13.68	21776/16445	12197
27-BF-1A	04815	April 21	17731-23489	-0.13-0.15	-6.14-5.53	-5.65-5.27	8.82-10.76	21812/18638	13839
28-BF-1B	04816		12880-18638	-0.30-0.07	-1.70-2.00	-0.69-4.18	0.50-7.88	21816/17073	12408
29-BF-1A	04829	April 22	11943-17701	-0.10-0.13	-5.75-5.21	-5.07-4.79	7.75-10.13	21410/16965	12673
30-BF-1B	04841		70431-76189	-0.05-0.48	-1.74-2.15	-2.79-1.90	1.11-5.06	21808/17047	12239
31-BF-1A	04855	April 23	75251-81009	-0.08-0.11	-4.88-5.03	-4.35-4.47	7.01-8.94	21788/15628	11904
32-BF-1B	04857		76159-81917	-0.10-0.29	-1.41-2.61	-4.09-1.59	0.55-7.36	21824/15892	11925
Total			-					690111/517226	397064
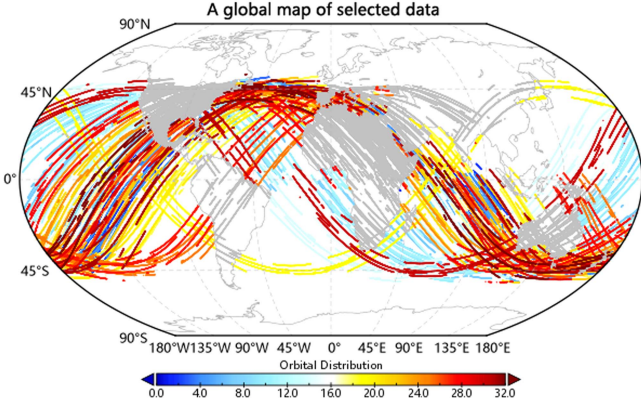
Fig. 3. Global map of selected data.
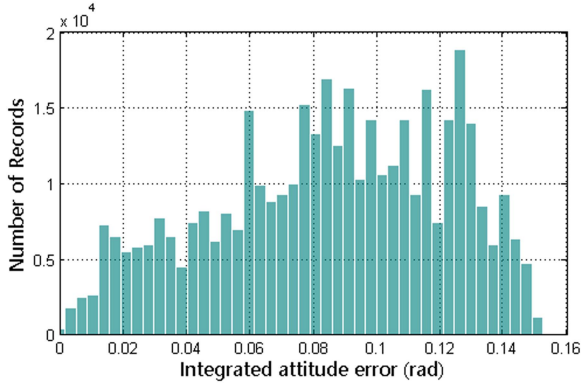
Fig. 4. Histogram of integrated attitude error distribution.

value is near 0 rad (0.0003°), the maximum value is 0.151 rad (8.65°), and the average value is 0.082 rad (4.70°).

3) ERA5 Re-Analysis Data: The European Center for Medium-range Weather Forecasts (ECMWF) 5th Generation (ERA5) reanalysis datasets (gridded with a spatial resolution of $0.25° \times 0.25°$ and temporal resolution of 1 h) is a global climate reanalysis assimilation product from various sources, including satellite and ground-based observations, available from 1979 until the present [30], [31]. These datasets are used to evaluate the ocean surface wind retrieval efficiency and indirectly reflects the effectiveness of the proposed algorithm. The ERA5 atmospheric variables include several surface wind parameters, of which the 10-m u and v components of the surface wind vector are used in the assessment of the BF-1 winds.

C. Methods

1) Theoretical Model: The bistatic scattering forward theoretical model, for which the original representation has been previously derived by Zavorotny and Voronovich [10], and the modified one were widely used in [22] and [25] and are expressed by the equation

$$P_{\hat{\tau},\hat{f}}^g = \frac{P^T \lambda^2}{(4\pi)^3} \iint_A G_{x,y}^T \sigma_{x,y}^0 G_{x,y}^R \left(R_{x,y}^R\right)^{-2}$$
$$\times \left(R_{x,y}^T\right)^{-2} \Lambda_{\hat{\tau};x,y}^2 S_{\hat{f};x,y}^2 dxdy. \quad (2)$$

where $P_{\hat{\tau},\hat{f}}^g$ is the received power of the reflected GNSS signal. Subscripts $(\hat{\tau}, \hat{f})$ denote the relative delays and Doppler frequencies. P^T is the transmit power of the GNSS signal. λ is the GNSS signal carrier wavelength. A is the ocean surface glistening zone, and subscripts (x, y) are the spatial physical coordinates of the scattering unit. $G_{x,y}^T$ is the gain of the transmitter antenna, and $G_{x,y}^R$ is the gain of the receive antenna. $R_{x,y}^T$ and $R_{x,y}^R$ are the transmitter to surface scattering unit and surface to receiver ranges, respectively. $\sigma_{x,y}^o$ is the NBRCS. $\Lambda_{\hat{\tau};x,y}$ is the signal correlation function in the delay, and $S_{\hat{f};x,y}$ is the signal SINC function in the frequency response.

The signal forward model above describes the GNSS signal power mapping from the physical (x, y) coordinates to the delay-Doppler coordinates, and the NBRCS can be extracted according to this formula. These delay-Doppler bins map nonuniquely spatially to the physical coordinates on the ocean surface. Therefore, the same DDM unit may correspond to several different physical scattering units far away. These physical units have nearly the same range loss (including R^T and R^R), but the antenna gain (including G^T and G^R) is obviously different due to the differences in physical coordinates.

To extract $\sigma0$, the following simplified expression is provided

$$\sigma_{\hat{\tau},\hat{f}}^0 = \frac{P_{\hat{\tau},\hat{f}}^g (4\pi)^3}{P^T \lambda^2 G_{sp}^T G_{sp}^R \left(R_{sp}^R\right)^{-2} \left(R_{sp}^T\right)^{-2} \overline{A}_{\hat{\tau},\hat{f}}} \quad (3)$$

where subscript *(sp)* is an abbreviation for specular point. $\overline{A}_{\hat{\tau},\hat{f}}$ is the effective scattering area and is obtained as

$$\overline{A}_{\hat{\tau},\hat{f}} = \iint_A \Lambda_{\hat{\tau};x,y}^2 S_{\hat{f};x,y}^2 dxdy. \quad (4)$$

All physical coordinates are approximated with their values at the specular point and applied across the entire DDM, except the effective area. Equation (3) shows that the accuracy of $\sigma0$ depends directly on the following key variables: transmit power P^T; transmit antenna gain G_{SP}^T; receive antenna gain G_{SP}^R; range loss; and effective scattering areas. Among these variables, the transmit power estimates and antenna gain maps or the effective isotropic radiated power could be generated by a ground-based GNSS power monitor or the zenith antenna navigation channels track and have been successfully implemented in [32], [33], and [34]. Additionally, the transmit antenna gain will vary from observation to observation, but will not be significantly affected due to its wider coverage than the receive antenna. The range loss, including the range from the transmitter to the surface and the surface to the receiver at the specular point, has an impact on the overall level of $\sigma0$, which can be corrected by improving the location estimation accuracy of the specular point. High accuracy surface specular point estimation using a highly accurate DTU10 mean sea surface height model and a refined specular point prediction algorithm has been successfully implemented by [25]. Scattering areas include the physical and effective scattering areas. The weights or convolution window scales of the spreading functions affect the accuracy and computational efficiency of effective scattering areas, which determine the accuracy of the DDM data. The accuracy of $\sigma0$ is much more
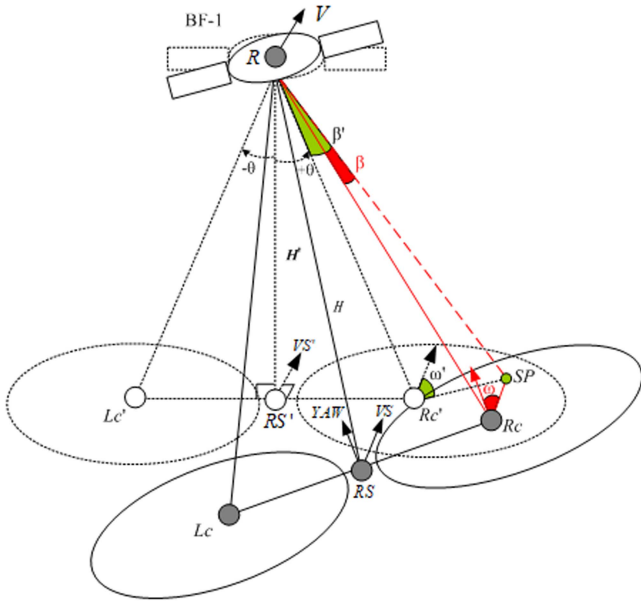
Fig. 5. Definition of the mapping angle of the specular point in the receive antenna pattern. The dashed line represents the ideal attitude case of the satellite platform, and the solid line represents the disturbance attitude.
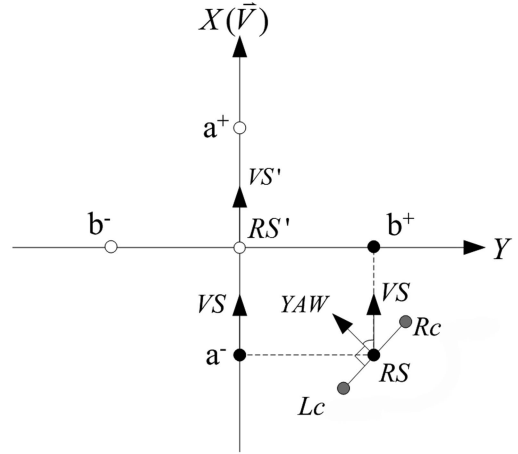

Fig. 6. Geometric relationship between attitudes angle of satellite platform and the ocean surface projection center of two receive antennas. In the satellite orbit coordinate system, the coordinate origin is selected at the centroid of the satellite, the X-axis represents the speed direction of the satellite, the Z-axis points to the center of the earth, and the Y-axis is orthogonal to the X-axis and Y-axis and satisfies the right-hand rule.

sensitive to the gain of the receive antenna than that of the above variables.

2) Receive Antenna Gain Calibration Algorithms: The off-nadir and azimuth angles were used to express the mapping of the specular point in the receive antenna pattern in the antenna coordinate system. Here, we define the nadir of an antenna as the projection position of the antenna beam center on the ocean surface (not the subsatellite point). In addition, the 0° (or 360°) azimuth is defined as the direction perpendicular to the line connecting the projection centers of two antennas and points to the forward direction of the satellite.

The earth centered earth fixed coordinate system was used here. The main lobe of the two antenna of the BF-1 pointing to $\pm\theta$ from the platform nadir symmetrically, of which the one with an angle of $+\theta$ is the starboard, and the other is the port one. As shown in Fig. 5, if the coordinate of the BF-1 satellite at a certain time is R, and the velocity vector is V, then the orbit height from the satellite to its subsatellite point is H', and the coordinate of one of the specular points is SP. When the satellite platform is in the ideal attitude, the coordinate of the subsatellite is RS', and the velocity vector is VS'; nadir of a starboard antenna is Rc', and the port one is Lc'. In the presence of attitude disturbance, the coordinates of the subsatellite is RS, and the velocity vector is VS; the orbit height is H, the nadir of a starboard antenna is Rc, and the port one is Lc. The subsatellite point in this article refers to the intersection of the Z-axis of the satellite and the ground in the satellite body coordinate system. Thus, the subsatellite point will change while the satellite attitude changes in pitch and roll.

Fig. 5 shows a significant difference in the mapping angles (off-nadir β and azimuth ω) of the specular point in the receive antenna pattern in the case of ideal and disturbance attitude.

The estimation of the ocean surface projection center of two receive antenna beams, which is the offset position after being disturbed by the platform attitude, is the core of the proposed algorithm. In this article, the pitch angle is defined as the rotation of the satellite body around the Y-axis, and the upward direction is positive. For example, as shown in Fig. 6, the new subsatellite point will fall in the a^+ direction when the pitch angle is positive; otherwise, it will fall in the opposite direction. Similarly, the roll angle is defined as the rotation around the X-axis, and the direction to the right is positive; the yaw angle is defined as the rotation around the Z-axis, and the direction to the right is positive. Fig. 6 shows the geometric relationship of the position deviation of the subsatellite point and the ocean surface projection center of the receive antennas when the angles of the pitch, roll, and yaw are negative, positive, and negative, respectively.

The receive antenna gain calibration algorithm is as follows. Let the satellite attitude parameters are u, v, and w, respectively.

1) The new coordinates of the subsatellite point are updated according to pitch attitude angle u and orbit height H'

$$\mathrm{RS}'' = \mathrm{RS}' + \frac{\mathrm{VS}'}{\mathrm{norm}\,(\mathrm{VS}')} * H' * \tan(u). \quad (5)$$

where RS'' is the new subsatellite point, $\mathrm{norm}(\cdot)$ represents the modulo operation, and the orbit height is updated as follows:

$$H'' = \mathrm{norm}\,(R - \mathrm{RS}''). \quad (6)$$

2) The subsatellite point and the orbit height are updated again according to roll attitude angle v, which is combined with the subsatellite point and orbit height calculated in the previous step

$$\mathrm{RS} = \mathrm{RS}'' - \frac{\mathrm{cross}\,(\mathrm{RS}'', \mathrm{VS}')}{\mathrm{norm}\,(\mathrm{cross}\,(\mathrm{RS}'', \mathrm{VS}'))} * H'' * \tan(v). \quad (7)$$

where $\text{cross}(\cdot)$ is represents the vector outer product, and the orbit height is updated as follows:

$$H = \text{norm}\,(R - \text{RS})\,. \tag{8}$$

3) Yaw vector YAW is obtained according to yaw attitude angle w and the subsatellite point (RS) calculated in the second step and calculated by rotating the velocity vector around the subsatellite point coordinate vector rotation axis by a certain yaw angle. The yaw vector is given as

$$\text{YAW} = (\text{RS} + \text{VS}) * M^T - \text{RS}. \tag{9}$$

where VS = VS', M^T represents the matrix transpose, and M is the rotation matrix and defined as (10) shown at the bottom of this page. where $\alpha = 1 - \cos(\text{yaw})$. m, n, and k are the elements of unit vector of the rotation axis RS and defined as follows:

$$\text{RS}_{\text{norm}} = [m, n, k] = \frac{\text{RS}}{\text{norm}\,(\text{RS})}\,. \tag{11}$$

4) Using the orthogonal relationship with yaw vector *YAW* and subsatellite point vector RS, the vector between the projection positions of the two antennas' beam center on the ocean surface is calculated by the vector outer product

$$\text{vect} = \text{cross}\,(\text{RS}, \text{YAW})\,. \tag{12}$$

The ocean surface projection center coordination of the starboard and the port antenna is calculated according to updated orbit height H, the beam pointing angle of receive antenna θ, and the right-hand rule

$$Rc = \text{RS} - \frac{\text{vect}}{\text{norm}\,(\text{vect})} * H * \tan(\theta) \tag{13}$$

$$Lc = RS + \frac{\text{vect}}{\text{norm}\,(\text{vect})} * H * \tan(\theta)\,. \tag{14}$$

5) Taking Fig. 5 as an example, the off-nadir was obtained based on the cosine relation of the vector angle

$$\beta = \arccos\left(\frac{\text{dot}\,(a, b)}{\sqrt{\text{dot}\,(a, a)} * \sqrt{\text{dot}\,(b, b)}}\right) \tag{15}$$

where $\text{dot}(\cdot)$ represents the vector inner product, and $a = $ SP-R and $b = Rc$-R represent different vectors.
Similarly, the azimuth is obtained as follows:

$$\omega = \arccos\left(\frac{\text{dot}\,(c, d)}{\sqrt{\text{dot}\,(c, c)} * \sqrt{\text{dot}\,(d, d)}}\right)\,. \tag{16}$$

where $c = $ SP-Rc and $d = $ YAW represents vectors.

6) According to the two angles obtained in the above steps, the calibrated receive antenna gain value can be obtained based on the receive antenna pattern. Then, the gain values

and their gain ratio before and after DDM calibration can be extracted from the antenna pattern

$$G\text{ratio}_i = \frac{G\text{ideal}_i}{G\text{dist}_i}\,. \tag{17}$$

where $G\text{ratio}_i$ is the gain ratio of the ith DDM, and $G\text{ideal}_i$ and $G\text{dist}_i$ are the gain values of the ith DDM under ideal attitude and attitude disturbance, respectively. Finally, to correct each DDM, each pixel is multiplied by the gain ratio of the image to obtain the calibrated DDM.

III. RESULTS

A. Changes of Mapping Angles

Owing to the attitude disturbance of the satellite platform, the mapping of the specular point of each DDM in the receive antenna pattern, including the off-nadir and azimuth angles, also changes significantly. Fig. 7 shows the changes of these angles in the first 1000 observations of orbits 04427 and 04429.

As explained, for each receive antenna in the BF-1 constellation, the relative antenna gain patterns were computed in 1° increments of their antenna beam center off-nadir and azimuth angles. To reduce the measurement noise, these relative antenna gain patterns were then smoothed over 3° windows in the off-nadir and azimuth angles. To satisfy the accuracy requirements of mapping, these antenna patterns were then interpolated using linear interpolation to a resolution of 0.1°.

Here, we also made grouping statistics based on these two orbits of data. The angle changes of the specular point mapping are counted according to the satellite and antenna types. The statistical result shows that the off-nadir angle changes within $\pm 3°$, except that the maximum deviation of the port antenna of BF-1B is 4.83°. In contrast, the azimuth deviation is much large.

B. Changes of Relative Receive Antenna Gain

Given that the mapping position of the specular point in the receive antenna patterns changes, the receive gain will also change. With the relative movement of the BF-1 and GNSS satellites, the specular point enters the antenna beam coverage area from the higher elevation angle areas (corresponding to lower gain) on the side of the satellite forward direction, enters the lower elevation angle areas (corresponding to higher gain) gradually, and finally exits from the higher elevation angle areas on the reverse side. Fig. 8 shows the above motion characteristics.

Here, we used two orbits (04427 and 04429) data to analyze the change in receive gain in different antenna modes. Fig. 8 shows that the receive gain difference of each DDM data is distributed within ± 0.2 in one orbit (gray areas in the figures). In addition, the gain change of BF-1B is more obvious than that of BF-1A, which may be due to the great attitude change of the

$$M = \begin{bmatrix} m*m*\alpha + \cos(w), & m*n*\alpha - k*\sin(w), & m*k*\alpha + n*\sin(w) \\ m*n*\alpha + k*\sin(w), & n*n*\alpha + \cos(w), & n*k*\alpha - m*\sin(w) \\ m*k*\alpha - n*\sin(w), & n*k*\alpha + m*\sin(w), & k*k*\alpha + \cos(w) \end{bmatrix} \tag{10}$$
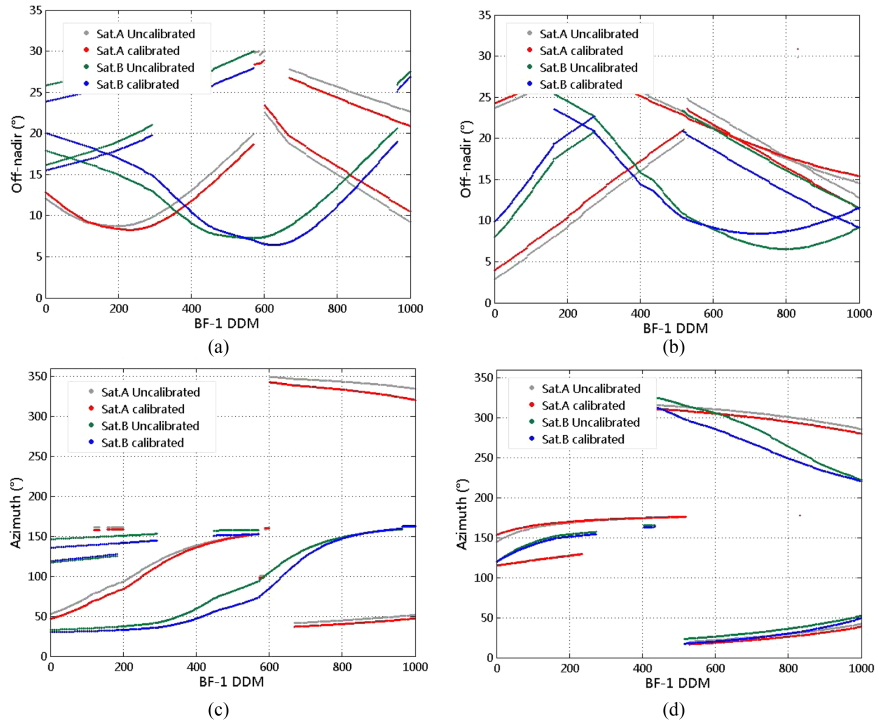
Fig. 7.   Change of mapping angle of the specular point in the receive antenna pattern with the data acquisition time. (a) and (c) Port antenna. (b) and (d) Starboard antenna.

TABLE II
PERFORMANCE METRICS OF WIND SPEED RETRIEVAL BASED ON THE ORIGINAL AND CALIBRATED $\sigma 0$

Satellite	Antenna	Original-based			Calibrated-based		
		RMSE (m/s)	MBE (m/s)	R	RMSE (m/s)	MBE (m/s)	R
BF-1A	Port	5.62	2.25	0.56	4.12	1.18	0.64
	Starboard	5.73	2.42	0.55	3.78	1.25	0.72
BF-1B	Port	4.68	1.41	0.66	3.26	1.02	0.73
	Starboard	4.74	1.46	0.61	3.19	0.88	0.75
Average		5.19	1.89	0.60	3.59	1.08	0.71

BF-1B satellite in this period, or related to the gain distribution of the receive antenna pattern.

C. Performance of Wind Speed Retrieval

To analyze the performance of the proposed algorithm, the accuracy analysis of the wind speed retrieval was carried out using the data before and after calibration. Three statistical metrics were selected to estimate the retrieval accuracy, including the RMSE, which is the most common method of comparison [35], the MBE, and the correlation coefficient (R).

First, all DDM data were matched to the ECMWF ERA5 10 m referenced reanalysis ocean surface wind speeds at the specular point within 0.25° and 30 min for the ground truth wind speed. These DDM data are not the data of the entire orbit, but the data located in the open ocean and within 30° off-nadir of the antenna beam center areas. We further controlled the quality of the data input into the GMF model and selected the data with a SNR not less than 3. Then, the calibrated $\sigma 0$ values were averaged in

the adjacent space before entered into the GMF wind retrieval model. For comparison, the uncalibrated original $\sigma 0$ values were spatially averaged and input into the same GMF wind retrieval model. These space adjacent (i.e., time adjacent) data refer to the same nadir antenna of the same satellite, and the signal is received from the same GNSS. The principle of spatial averaging is as follows.

1) Five adjacent $\sigma 0$ values are selected when the incident angle is less than or equal to 20°.
2) Three adjacent $\sigma 0$ values are selected when the incident angle is greater than 20°, but less than or equal to 42°.
3) The average is not obtained when the incident angle exceeds 42°.

Wind speed retrieval is carried out based on calibrated $\sigma 0$ and uncalibrated $\sigma 0$, and the retrieval results are compared with the ERA5 referenced wind speed for error analysis. According to different satellites and their receive antennas, the experimental datasets are divided into four groups, and the performance of wind speed retrieval is tested in different groups. Table II gives
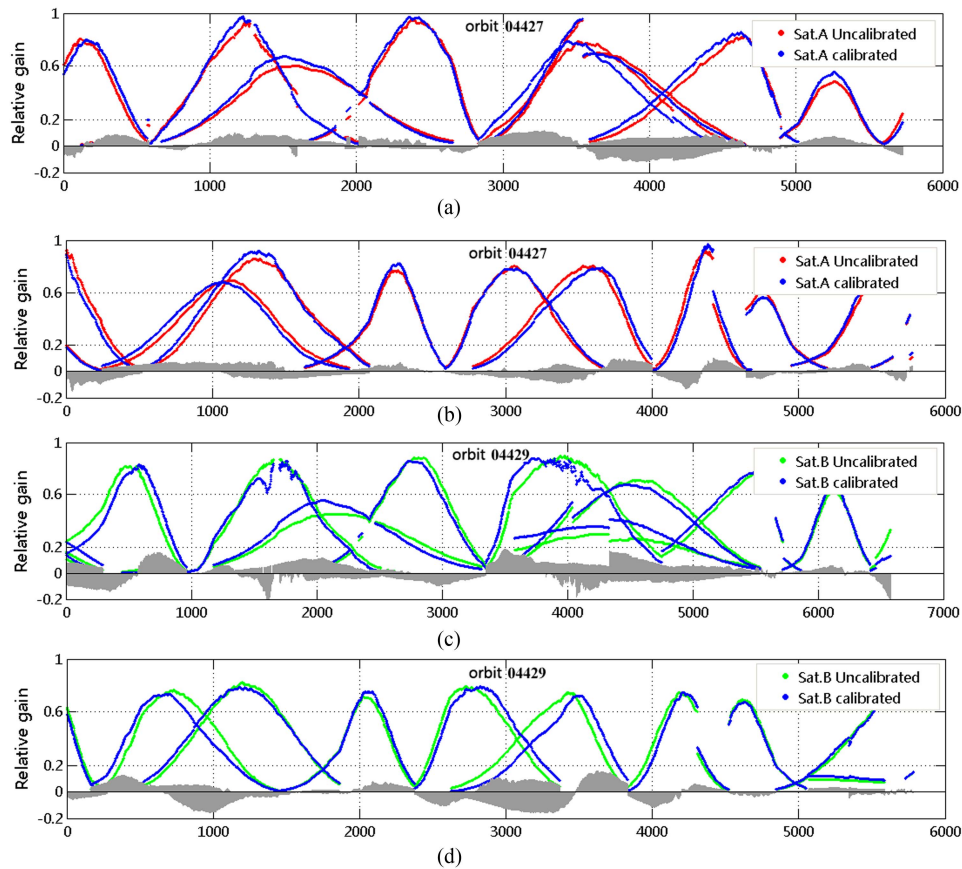
Fig. 8. Time series of the relative receive gain changes and its deviation, where: (a) the port antennas of BF-1A; (b) the starboard antennas of BF-1A; (c) the port antennas of BF-1B; and (d) the starboard antennas of BF-1B.

the statistical results of wind speed retrieval error using the three statistical metrics.

Table II gives that the proposed data calibration algorithm reduces the error of the wind speed retrieval to varying degrees in each groups. According to the average results, RMSE and MBE decreased by 30.91% and 42.57%, respectively, while the correlation coefficient (R) increased by 19.33%. In addition, the datasets used here are greatly disturbed by the attitude of the satellite platform, so the overall retrieval accuracy is low.

IV. DISCUSSION

A. Comparison of Wind Speed Retrieval Error and Platform Attitude Disturbance

On the basis of uncalibrated and calibrated experimental data, we carried out wind speed retrieval error statistics and correlated the above errors with the platform attitude disturbance. In fact, the wind speed retrieval errors include positive, negative, and zero errors. Here, we take the absolute values of all the errors for statistical convenience. Fig. 9 shows that the impact of the satellite platform attitude disturbance on wind speed retrieval is obvious, and most of the data with a large retrieval error can be attributed to the large platform attitude disturbance. In addition, the influence of the satellite platform attitude disturbance on

wind speed retrieval is abated significantly after calibration. In particular, the wind speed retrieval error of the data with a large attitude disturbance is significantly reduced.

To evaluate the relationship between wind speed retrieval error and attitude disturbance, the attitude disturbance is evenly divided into 20 error intervals, and the accuracy of wind speed retrieval is analyzed by using the RMSE, MBE, and correlation coefficient (R) in each interval. Fig. 10 shows that the proposed data calibration algorithm is effective in reducing the wind speed retrieval error, especially when the data is greatly disturbed by the attitude of the satellite platform.

Taking the RMSE as an example, when the integrated attitude error is within 0.025 rad, the wind speed retrieval error using the original data can be maintained at approximately 3 m/s, but when the integrated attitude error exceeds this range, the wind speed retrieval error sharply increases. This phenomenon also explains the low accuracy of the overall wind speed retrieval based on the original data. When wind speed retrieval is carried out based on the calibrated data, the retrieval accuracy does not change significantly in the low attitude disturbance interval. However, the retrieval accuracy is significantly improved with the increase of the platform attitude disturbance. The other two indicators also reflect that the accuracy of the wind speed retrieval based on calibrated data significantly improved.
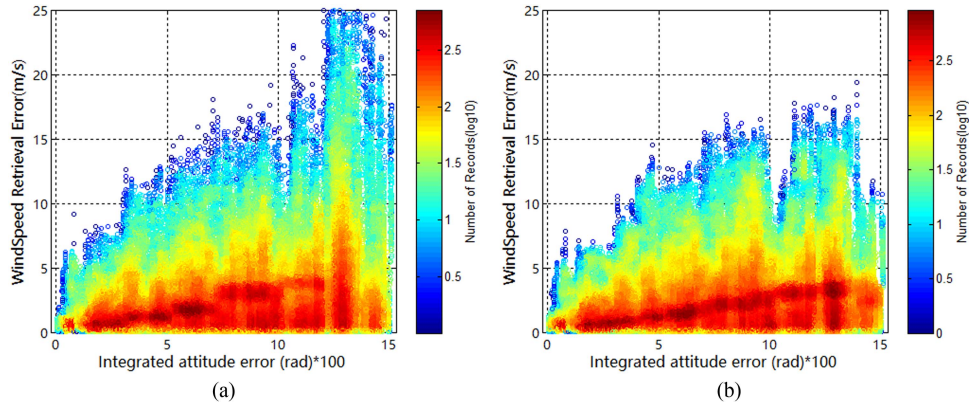
Fig. 9.   Scatter-plot relationship between the integrated attitude error and wind speed retrieval error based on (a) uncalibrated and (b) calibrated data. The color density represents the log10 of the number density of observation points.
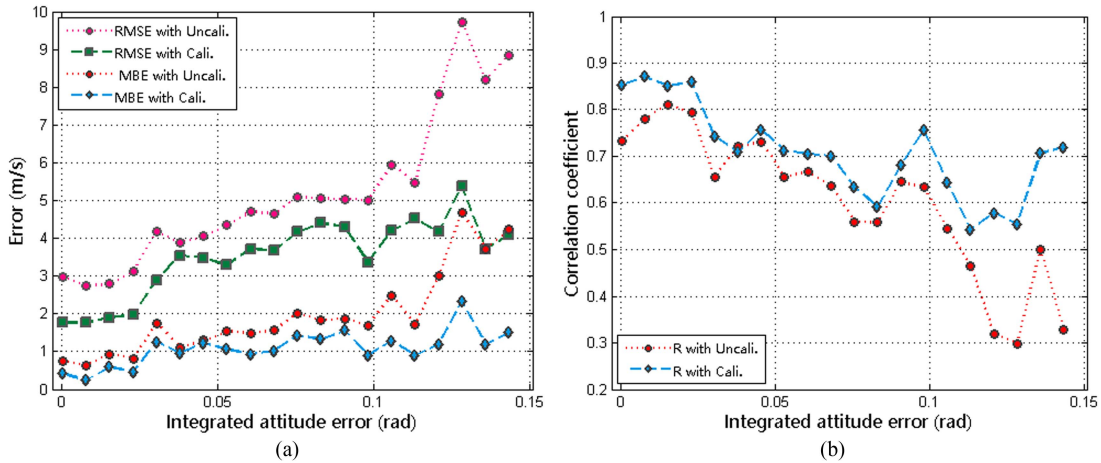

Fig. 10.   Error distribution of wind speed retrieval results under different attitude disturbances using un-calibrated and calibrated data. (a) RMSE and MBE. (b) Correlation coefficient (R).

B. Comparison of Wind Speed Retrieval Error and Wind Speed Range

The maximum ERA5 referenced wind speed corresponding to the experimental data used here is 27.18 m/s, and the minimum is 0.04 m/s. Therefore, the reference wind speed is divided into 27 intervals in the order of natural numbers, and the RMSE is used for the accuracy statistics of the wind speed retrieval in each interval. Fig. 11(a) shows that the wind speed retrieval accuracy based on the calibrated data is significantly better than the original data.

The retrieval error is generally positively correlated with the reference wind speed, that is, the higher the wind speed is, the greater the retrieval error is. However, we cannot conclude from our results that wind retrieval error fully conforms to the above law. We use the quartile box plot and the mean value to comprehensively analyze the platform attitude disturbance corresponding to each wind speed interval, and the results are shown in Fig. 11(b). The combination of the two subgraphs indicates a certain correlation between the wind speed extraction

error and the satellite platform attitude disturbance. In general, in the lower wind speed range (less than 10 m/s), the satellite attitude disturbance shows an increasing trend (the box diagram is more obvious), and the wind speed retrieval error increases accordingly. In the middle wind speed range (greater than 10 m/s and less than 15 m/s), the satellite attitude disturbance is gradually mild, and the wind speed retrieval error also decreases. In the high wind speed range (greater than 16 m/s), the satellite attitude disturbance shows the trend of alternating rise and fall, and the wind speed retrieval error also changes irregularly and shows an overall increase. This finding also shows that the accuracy of wind speed retrieval is obviously affected by the attitude disturbance of the satellite platform. In addition, Fig. 11(a) shows that although the retrieval accuracy is significantly improved after attitude calibration, the trend of retrieval error is still affected by the attitude and cannot be completely eliminated, which may be related to other factors, such as the GMF empirical model.

The comparison of the improvement of wind speed retrieval under different satellite platform attitude disturbances and wind speed ranges shows that the proposed method can effectively
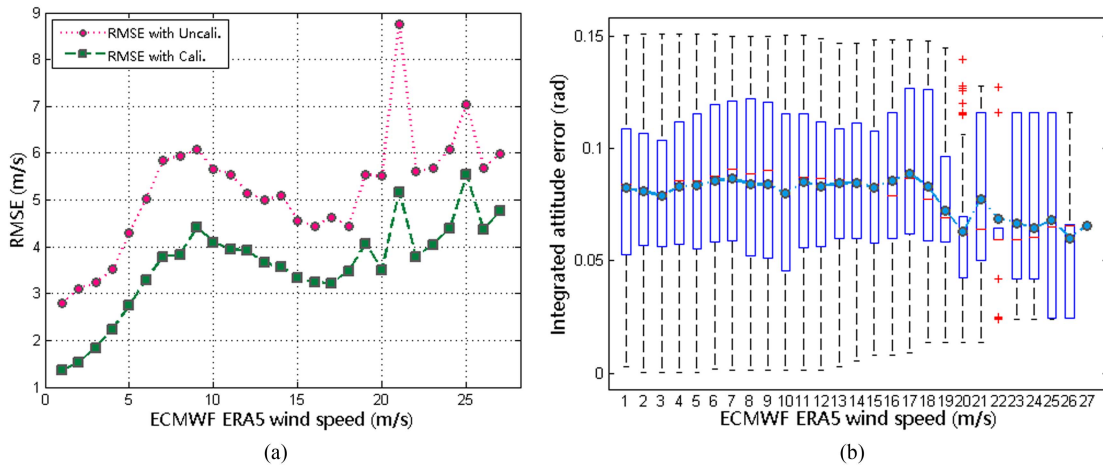
Fig. 11. Relationship between wind speed retrieval error and satellite platform attitude disturbance under different wind speed range. (a) RMSE statistics using $\sigma 0$ with uncalibrated and calibrated. (b) Corresponding platform attitude error statistics using quartile box plot and mean value (the blue dots).

improve the quality of data affected by the satellite platform attitude disturbances and then improve the accuracy of ocean wind speed retrieval. Given that the attitude of the satellite platform has a certain disturbance, this method can be used to improve the full mission's data with roll-pitch-yaw variations.

However, although the retrieval accuracy is significantly improved after data calibration, the wind speed retrieval error is still correlated with the satellite platform attitude disturbance and cannot be completely eliminated even if the correlation is very weak. In addition to platform attitude, additional factors might also play a significant role in the wind speed retrieval process, including the training samples used in the GMF wind retrieval model. Subsequently, to reduce the correlation between wind speed retrieval error and platform attitude disturbance and achieve a more robust ocean wind speed retrieval performance, further work is still needed to retrain the retrieval GMF on the basis of the calibrated datasets. In addition, the use of integrated attitude disturbance to characterize the attitude of the satellite platform to analyze the wind speed retrieval error, the specific platform attitude and its influence on the retrieval error should be explored in the future. Furthermore, the maximum ERA5 referenced wind speed corresponding to the experimental data used in this article is approximately 27 m/s, and the amount of high wind speed data is relatively low. On the one hand, few high winds exist. On the other hand, this article also limits the data with SNR lower than 3, and high winds generally correspond to low SNR, which also indirectly leads to the reduction of the high winds data. In future work, the high wind speed regime will be the focus of interest, and with the introduction of more experimental data, especially high wind speed data, the wind speed retrieval performance of the proposed algorithm at different wind speeds could be further evaluated.

High quality GNSS-R measurements will be used for a better understanding of global weather abnormalities and to generally improve weather forecasting. To improve the performance of the proposed calibration algorithm and obtain high quality measurements, necessary preparations, including but not limited to the following two, and a general recommendation for future

GNSS-R missions of BF-1 satellite are needed. First, continuous and high-precision satellite platform attitude data should be an absolute priority to ensure that the location of the specular point in the antenna footprint (i.e., receive gain pattern) can be accurately determined. Currently, the attitude data of the BF-1 satellite platform is sampled and not continuous. For an attitude data with a large sampling interval, such as several hours interval, the platform attitude interpolation in this period will be inaccurate, resulting in large errors in the antenna gain calculation at the specular point. Second, the nadir GNSS-R antenna gain patterns should be characterized well before launch and during on-orbit operation to accurately estimate the antenna gain at the specular point.

V. CONCLUSION

This article proposes a data calibration method for receive antenna gain correction using satellite platform attitude measurements, and systematically evaluates the improvement effect of the proposed calibration algorithm on the accuracy of wind speed retrieval from the perspectives of data acquisition source, platform attitude disturbance, and wind speed range. A total of 32 orbits DDM data, which were greatly disturbed by the attitude, are selected to test the effectiveness of the proposed algorithm. The accuracy of wind speed retrieval based on uncalibrated and calibrated data is analyzed, and the results show the following: the impact of satellite platform attitude disturbance on wind speed retrieval accuracy is generally obvious, and most of the data with a large retrieval error are contributed by the large platform attitude disturbance; and the influence of the satellite platform attitude disturbance on wind speed retrieval is abated significantly after data calibration, especially when the data is greatly disturbed by the attitude of the satellite platform. In terms of average retrieval accuracy, the RMSE and MBE decreased by 30.91% and 42.57%, respectively, after data calibration, while the correlation coefficient between the retrieval of wind speed and the ECMWF ERA5 reference increased by 19.33%.

References

[1] Q. Peng and S. Jin, "Significant wave height estimation from space-borne cyclone GNSS reflectometry," *Remote Sens.*, vol. 11, 2019, Art. no. 584.

[2] A. Kirincich, "Remote sensing of the surface wind field over the coastal ocean via direct calibration of HF radar backscatter power," *J. Atmos. Ocean. Technol.*, vol. 33, pp. 1377–1392, 2016.

[3] X. Li, D. Yang, J. Yang, G. Han, G. Zheng, and W. Li, "Validation of NOAA CYGNSS wind speed product with the CCMP data," *Remote Sens.*, vol. 13, 2021, Art. no. 1832.

[4] M. B. Christiansen, W. Koch, J. Horstmann, C. B. Hasager, and M. Nielsen, "Wind resource assessment from C-band SAR," *Remote Sens. Environ.*, vol. 105, pp. 68–81, 2006.

[5] D. Mayers and C. S. Ruf, "Tropical cyclone center fix using CYGNSS winds," *J. Appl. Meteor. Climatol.*, vol. 58, pp. 1993–2003, 2019.

[6] J. A. Crespo, D. J. Posselt, and S. Asharaf, "CYGNSS surface heat flux product development," *Remote Sens.*, vol. 11, 2019, Art. no. 2294.

[7] R. Tang, D. Liu, G. Han, Z. Ma, and B. D. Young, "Reconstructed wind fields from multi-satellite observations," *Remote Sens.*, vol. 6, pp. 2898–2911, 2014.

[8] T. Hu, Y. Li, Y. Li, Y. Wu, and D. Zhang, "Retrieval of sea surface wind fields using multi-source remote sensing data," *Remote Sens.*, vol. 12, 2020, Art. no. 1482.

[9] A. A. Arroyo et al., "Dual-polarization GNSS-R interference pattern technique for soil moisture mapping," *IEEE J. Sel. Topics Appl. Earth Observ. Remote Sens.*, vol. 7, no. 5, pp. 1533–1544, May 2014, doi: 10.1109/JSTARS.2014.2320792.

[10] V. U. Zavorotny and A. G. Voronovich, "Scattering of GPS signals from the ocean with wind remote sensing application," *IEEE Trans. Geosci. Remote Sens.*, vol. 38, no. 2, pp. 951–964, Mar. 2000.

[11] C. D. Bussy-Virat, C. S. Ruf, and A. J. Ridley, "Relationship between temporal and spatial resolution for a constellation of GNSS-R satellites," *IEEE J. Sel. Topics Appl. Earth Observ. Remote. Sens.*, vol. 12, no. 1, pp. 16–25, Jan. 2018, doi: 10.1109/JSTARS.2018.2833426.

[12] S. Jin and A. Komjathy, "GNSS reflectometry and remote sensing: New objectives and results," *Adv. Space Res.*, vol. 46, pp. 111–117, 2010.

[13] C. S. Ruf et al., "A new paradigm in earth environmental monitoring with the CYGNSS small satellite constellation," *Sci. Rep.*, vol. 8, 2018, Art. no. 8782.

[14] C. D. Hall and R. A. Cordey, "Multistatic scatterometry," in *Proc. IEEE Int. Geosci. Remote Sens. Symp.*, 1988, vol. 1, pp. 561–562.

[15] M. Unwin, S. Gleason, and M. Brennan, "The space GPS reflectometry experiment on the U.K. disaster monitoring constellation satellite," in *Proc. ION-GPS/GNSS*, 2003, pp. 2656–2663.

[16] S. Gleason et al., "Detection and processing of bistatically reflected GPS signals from low earth orbit for the purpose of ocean remote sensing," *IEEE Trans. Geosci. Remote Sens.*, vol. 43, no. 6, pp. 1229–1241, Jun. 2005, doi: 10.1109/TGRS.2005.845643.

[17] M. Unwin, P. Jales, J. Tye, C. Gommenginger, G. Foti, and J. Rosello, "Spaceborne GNSS-reflectometry on TechDemoSat-1: Early mission operations and exploitation," *IEEE J. Sel. Topics Appl. Earth Observ. Remote Sens.*, vol. 9, no. 10, pp. 4525–4539, Oct. 2016, doi: 10.1109/JSTARS.2016.2603846.

[18] C. S. Ruf et al., "New ocean winds satellite mission to probe hurricanes and tropical convection," *Bull. Amer. Meteorol. Soc.*, vol. 97, pp. 385–395, 2016.

[19] Y. Krien et al., "Can we improve parametric cyclonic wind fields using recent satellite remote sensing data?," *Remote Sens.*, vol. 10, 2018, Art. no. 1963.

[20] C. Jing, X. Niu, C. Duan, F. Lu, and X. Yang, "Sea surface wind speed retrieval from the first Chinese GNSS-R mission: Technique and preliminary results," *Remote Sens.*, vol. 11, 2019, Art. no. 3013.

[21] S. Gleason, A. O'Brien, A. Russel, M. M. Al-Khaldi, and J. T. Johnson, "Geolocation, calibration and surface resolution of CYGNSS GNSS-R land observations," *Remote Sens.*, vol. 12, 2020, Art. no. 1317.

[22] R. Balasubramaniam and C. S. Ruf, "Neural network based quality control of CYGNSS wind retrieval," *Remote Sens.*, vol. 12, 2020, Art. no. 2859.

[23] M. P. Clarizia and C. S. Ruf, "Wind speed retrieval algorithm for the cyclone global navigation satellite system (CYGNSS) mission," *IEEE Trans. Geosci. Remote Sens.*, vol. 54, no. 8, pp. 4419–4432, Aug. 2016, doi: 10.1109/TGRS.2016.2541343.

[24] C. S. Ruf and R. Balasubramaniam, "Development of the CYGNSS geophysical model function for wind speed," *IEEE J. Sel. Topics Appl. Earth Observ. Remote Sens.*, vol. 12, no. 1, pp. 66–77, Jan. 2019, doi: 10.1109/JSTARS.2018.2833075.

[25] S. Gleason, C. S. Ruf, A. J. O'Brien, and D. S. McKague, "The CYGNSS level 1 calibration algorithm and error analysis based on on-orbit measurements," *IEEE J. Sel. Topics Appl. Earth Observ. Remote Sens.*, vol. 12, no. 1, pp. 37–49, Jan. 2019. doi: 10.1109/JSTARS.2018.2832981.

[26] M. L. Hammond, G. Foti, C. Gommenginger, and M. Srokosz, "Temporal variability of GNSS-reflectometry ocean wind speed retrieval performance during the U.K. TechDemoSat-1 mission," *Remote Sens. Environ.*, vol. 242, 2020, Art. no. 111744.

[27] J. Reynolds, M. P. Clarizia, and E. Santi, "Wind speed estimation from CYGNSS using artificial neural networks," *IEEE J. Sel. Topics Appl. Earth Observ. Remote Sens.*, vol. 13, pp. 708–716, 2020, doi: 10.1109/JSTARS.2020.2968156.

[28] X. Li et al., "Analysis of coastal wind speed retrieval from CYGNSS mission using artificial neural network," *Remote Sens. Environ.*, vol. 260, 2021, Art. no. 112454.

[29] B. Wan, X. Niu, C. Jing, B. Lei, and C. Han, "Calibration and error analysis of the BF-1 demonstration GNSS-R satellites," in *Proc. China Satell. Navig. Conf., Volume I*, 2020, vol. 650, pp. 196–205.

[30] M. Asgarimehr, I. Zhelavskaya, G. Foti, S. Reich, and J. Wickert, "A GNSS-R geophysical model function: Machine learning for wind speed retrievals," *IEEE Geosci. Remote Sens. Lett.*, vol. 17, no. 8, pp. 1333–1337, Aug. 2020, doi: 10.1109/LGRS.2019.2948566.

[31] M. B. Rivas and A. Stoffelen, "Characterizing ERA-interim and ERA5 surface wind biases using ASCAT," *Ocean Sci.*, vol. 15, pp. 831–852, 2019.

[32] T. Wang, C. S. Ruf, B. Block, and D. McKague, "Characterization of the transmit power and antenna pattern of the GPS constellation for the CYGNSS mission," in *Proc. IEEE Int. Geosci. Remote Sens. Symp.*, 2018, pp. 4011–4014, doi: 10.1109/IGARSS.2018.8518531.

[33] T. Wang, C. S. Ruf, B. Block, D. S. McKague, and S. Gleason, "Design and performance of a GPS constellation power monitor system for improved CYGNSS L1B calibration," *IEEE J. Sel. Topics Appl. Earth Observ. Remote Sens.*, vol. 12, no. 1, pp. 26–36, Jan. 2019, doi: 10.1109/JSTARS.2018.2867773.

[34] T. Wang, C. Ruf, S. Gleason, B. Block, D. McKague, and A. O'Brien, "A real-time EIRP level 1 calibration algorithm for the CYGNSS mission using the zenith measurements," in *Proc. IEEE Int. Geosci. Remote Sens. Symp.*, 2019, pp. 8725–8728, doi: 10.1109/IGARSS.2019.8900456.

[35] C. S. Ruf, S. Gleason, and D. S. McKague, "Assessment of CYGNSS wind speed retrieval assessment," *IEEE J. Sel. Topics Appl. Earth Observ. Remote Sens.*, vol. 12, no. 1, pp. 87–97, Jan. 2019, doi: 10.1109/JSTARS.2018.2825948.

Chenxin Chen was born in Tengzhou, China, in 1983. He received the Ph.D. degree in signal and information processing from University of Chinese Academy of Sciences, Beijing, China, in 2013.

His current work focuses on various aspects of calibration and validation for the BF-1 GNSS-R mission. His primary research focus is currently in the area of GNSS-R remote sensing theory, ocean geophysical retrieval algorithm development, and GNSS-R remote sensing applications. His other research activities include optical remote sensing image processing and classification.

Xiaoyu Wang received the Ph.D. degree in mechanical and electrical engineering from Harbin institute of Technology, Harbin, China, in 2007.

He was a Satellite Systems Engineer with the China Academy of Space Technology, Beijing, China. He was involved in remote sensing with an emphasis on the development of space-borne remote sensing hardware, calibration techniques, and on mathematical inversion techniques for geophysical retrievals.

Zhao Bian received the M.S. and Ph.D. degrees in signal and information processing from the University of Chinese Academy of Sciences, Beijing, China, in 2011 and 2020, respectively.

Her current research interests include data analysis, machine learning and statistical processing.

Dongdong Fan received the Ph.D. degree in photoelectric engineering from the Department of Precision Instrument, Tsinghua University, Beijing, China, in 2003.

His work has focused on mathematical inversion techniques for geophysical retrievals.

Haoyun Wei received the Ph.D. degree in photoelectric engineering from the Department of Precision Instrument, Tsinghua University, Beijing, China, in 2007.

His research interests include GNSS-R remote sensing, ocean geophysical retrieval algorithm development, statistical signal processing, and data analysis.

Zhaoguang Bai received the B.S. and M.S. degrees in aircraft design from Beijing Institute of Technology, Beijing, China, in 1985 and 1988, respectively.

He is currently a Professor of Aircraft Design with China Academy of Space Technology, Beijing, China, and a Principal Investigator of the BF-1 GNSS-R Mission. His research interests include microsatellite system design, and technology development.